Biophysical *Journal*
Article

Biophysical Society

FBP21's C-Terminal Domain Remains Dynamic When Wrapped around the c-Sec63 Unit of Brr2 Helicase

Jana Sticht,[1,2,*] Miriam Bertazzon,[1] Lisa M. Henning,[1] Jan R. Licha,[1] Esam T. Abualrous,[1,3] and Christian Freund[1,*]
[1]Laboratory of Protein Biochemistry, [2]Core Facility BioSupraMol, and [3]Computational Molecular Biology Group, Freie Universität Berlin, Berlin, Germany

ABSTRACT Based on our recent finding that FBP21 regulates human Brr2 helicase activity involved in the activation of the spliceosomal B-complex, we investigated the structural and dynamic contribution of FBP21 to the interaction. By using NMR spectroscopy, we could show that the 50 C-terminal residues of FBP21 (FBP21$^{326–376}$), which are sufficient to fully form the interaction with the C-terminal Sec63 unit of Brr2 (Brr2$^{\text{C-Sec63}}$), adopt a random-coil conformation in their unbound state. Upon interaction with Brr2$^{\text{C-Sec63}}$, 42 residues of FBP21$^{326–376}$ cover the large binding site on Brr2$^{\text{C-Sec63}}$ in an extended conformation. Short charged motifs are steering complex formation, still allowing the bound state to retain dynamics. Based on fragment docking in combination with experimental restraints, we present models of the complex structure. The FBP21$^{326–376}$/Brr2$^{\text{C-Sec63}}$ interaction thus presents an example of an intrinsically disordered protein/ordered-protein interaction in which a large binding site provides high specificity and, in combination with conformational disorder, displays a relatively high affinity.

INTRODUCTION

Proteins present a variable amount of conformational plasticity ranging from stably folded domains over compact but unstructured molten globules to highly extended unstructured states (intrinsically disordered proteins (IDPs)). Many proteins combine several of these elements in a modular architecture, comprising stably folded domains flexibly linked to each other and/or to intrinsically disordered protein regions (IDPRs). Additionally, the folded domains can still experience local unfolding, and unstructured parts can have the propensity to adopt secondary structure (1). Upon interaction with a binding partner, disordered proteins can become part of rigid complexes, often resulting from disorder-to-order transitions in the IDP. This is accompanied by a high entropic penalty, which can be reduced by motifs with a transient propensity to fold (molecular recognition features (MoRFs)). Additionally, IDPs can also become part of so-called fuzzy complexes, in which the IDP retains its dynamic nature to a large extent. Fuzziness in protein-protein complexes can result from different situations (2): the part of the IDP/IDPR that interacts is rigidly bound, but linker sequences (clamp model) or terminal sequences (flanking model) retain fast dynamic properties. Alternatively, the IDP/IDPR is not rigidly bound but samples different conformations of a bound state (polymorphic model) or even binds to different sites (random model).

These variable states of order in the free and bound state of proteins forming a complex involve dynamics on a wide range of timescales and influence the entropic and enthalpic contributions in protein-protein interactions, finally defining affinity and specificity.

IDPs or IDPRs are involved in a wealth of cellular processes (1,3). They often act as scaffolds in macromolecular complexes or interaction networks, facilitating signal integration and localization. IDPs have been shown to cover large interfaces on their folded interaction partners as compared to their size (4). This provides high specificity and the potential of high affinity, depending on entropy and enthalpy contributions. The variable loss in large intrinsic conformational entropy upon binding modulates the interaction affinity. Complexes involving IDPs thus often have relatively fast association and dissociation kinetics, which is favorable for highly dynamic processes that depend on more transient interactions.

Submitted May 23, 2018, and accepted for publication November 19, 2018.

*Correspondence: sticht@zedat.fu-berlin.de or chfreund@zedat.fu-berlin.de

Editor: Michael Sattler.
https://doi.org/10.1016/j.bpj.2018.11.3123

One prominent example of such a dynamic process is pre-messenger RNA splicing. The stepwise de novo assembly of the spliceosome on the pre-messenger RNA substrate in particular depends on the transient interactions of regulatory proteins with core spliceosomal proteins. Accordingly, the accessory spliceosomal proteins are more disordered than the core proteins actually catalyzing the reaction (5). Accessory proteins act in all steps of spliceosome assembly, including the binding of the U1 and U2 small nuclear ribonuclear ribonucleoproteins (snRNPs) to the 5′ splice site and branch point sequence (A-complex formation), the recruitment of the U4/U6.U5 tri-snRNP (B-complex formation), and spliceosomal activation (formation of the B^{act} and B* complexes) (6). The RNA helicase Brr2 is a key player in the transition from the B to the B^{act} complex because it unwinds the U4/U6 small nuclear RNA (snRNA) duplex, releasing the U4 snRNP. This enables U6 snRNA to basepair with U2 snRNA and form a catalytically important intramolecular stem loop (7,8). The unwinding of the U4/U6 di-snRNA leads to the formation of the catalytic core of the spliceosome, and the irreversible loss of the U4 snRNP is believed to fix splice site choice. This process is therefore of particular importance for alternative splicing decisions and quality control and calls for tight regulation.

We recently discovered that the intrinsically disordered C-terminal domain of FBP21 ($FBP21^{200–376}$) regulates the function of human Brr2 RNA helicase by uncoupling the activating function of the catalytically inactive Brr2 C-cassette ($Brr2^{CC}$) from the unwinding activity of the Brr2 N-cassette ($Brr2^{NC}$) (9). Although the inhibitory function of the interaction seems to depend on additional contacts, the interaction of FBP21 and Brr2 was shown to be mediated to a large extent through binding of the C-terminal 50 amino acids of FBP21 ($FBP21^{326–376}$) to the Sec63 unit of $Brr2^{CC}$ ($Brr2^{C\text{-}Sec63}$) (9). Even though the $FBP21^{326–376}$/$Brr2^{C\text{-}Sec63}$ interaction does not include the catalytically active N-cassette and lacks additional contacts, it covers a large interface and displays a relatively high affinity ($K_D = 0.11 \pm 0.001$ μM) (9). The $FBP21^{326–376}$/$Brr2^{C\text{-}Sec63}$ interaction was well described on the site of Brr2 (9), but the contribution of FBP21 residues to the interface as well as the conformational behavior of $FBP21^{326–376}$ upon binding still remained elusive. The recently published cryo-electron microscopy structure of a precatalytic human B-complex (10) added evidence that FBP21 prevents Brr2 from unwinding of the U4/U6 di-snRNA, but the C-terminal region of FBP21 was invisible in the EM structure and thus could not provide novel information about the FBP21-Brr2 interaction. Here, we describe that $FBP21^{326–376}$ adopts an extended conformation to wrap around the $Brr2^{C\text{-}Sec63}$ unit. The interface incorporates nearly the entire length of the FBP21 fragment without completely losing its flexibility, resulting in a dynamic complex with relatively high affinity. We propose models of the complex structure that are overall consistent with the experimental data and postulate that this interface provides a platform for regulation.

MATERIALS AND METHODS

Protein expression and purification

Human $FBP21^{326–376}$ (residues 326–376) and human $Brr2^{C\text{-}Sec63}$ (residues 1840–2136) were expressed and purified as described previously (9). Four $FBP21^{326–376}$ mutants were cloned using quick-change mutagenesis PCR. In $FBP21^{GGG}$, residues KVV at position 334–336 are replaced by GGG. $FBP21^{ANLA}$ contains the substitutions R367A and R370A. Two further point mutations were prepared ($FBP21^{S344C}$ and $FBP21^{S366C}$), each containing a substitution from serine to cysteine for spin labeling. Isotope-labeled proteins for NMR were produced in *Escherichia coli* using M9 minimal medium and $^{15}N\text{-}NH_4Cl$. To obtain $^2H\text{-}^{15}N\text{-}^{13}C\text{-}FBP21^{326–376}$, $^2H\text{-}^{13}C$-glucose was also used, and the medium was based on D_2O.

NMR spectroscopy

All NMR spectra were recorded on a Bruker Avance III 700 MHz spectrometer (Bruker, Billerica, MA) equipped with a 5 mm triple resonance cryoprobe. Spectra were processed using TopSpin3.2 (Bruker) and analyzed using CcpNMR Analysis 2.4.2 (11). TROSY-based heteronuclear single quantum coherence (HSQC) and triple resonance spectra were recorded for either 140 μM $^2H^{15}N^{13}C\text{-}FBP21^{326–376}$ (HNCA, HNCACB (25% nonuniform sampling [NUS]), HNCO (35% NUS), HN(CA)CO (30% NUS)) or 140 μM $^2H^{15}N^{13}C\text{-}FBP21^{326–376}$ with a threefold molar excess of unlabeled $Brr2^{C\text{-}Sec63}$ (HNCA (65% NUS), HN(CO)CA (50% NUS), HNCACB (45% NUS), HNCO (29% NUS)) in 20 mM NaP (pH 6.5), 100 mM NaCl with 10% D_2O at 300 K. Backbone assignments for $FBP21^{326–376}$ in the free and $Brr2^{C\text{-}Sec63}$-bound state were obtained by using CcpNMR Analysis (11) and were deposited to the Biological Magnetic Resonance Bank (BMRB) with accession codes 27629 and 27630, respectively.

$^1H\text{-}^{15}N$-NOESY-HSQC spectra (80 ms mixing time) of 140 μM $^2H^{15}N^{13}C\text{-}FBP21^{326–376}$ without or with a threefold molar excess of $Brr2^{C\text{-}Sec63}$ were used to detect backbone H^N-H^N-NOEs as indicators of structural order.

^{15}N relaxation experiments were performed with 125 μM $^{15}N\text{-}FBP21^{326–376}$ without or with a threefold molar excess of unlabeled $Brr2^{C\text{-}Sec63}$. $^1H\text{-}^{15}N$-heteronuclear Overhauser effects (NOE) were measured by interleaved pseudo-three-dimensional (3D) experiments using a relaxation delay of 8 s in the reference experiment or 2 s plus 4 s saturation consisting of 180 repetitions of a 22 ms (delay-180° pulse-delay) sequence. Presented is the average of three independent measurements; error bars reflect the SD. Relaxation times were measured by interleaved pseudo-3D experiments applying temperature compensation with a relaxation delay of 2 s in T_2 and 3.5 s in T_1 experiments. T_1 and T_2 times and their uncertainties were obtained from exponential fits of decaying peak intensities by using CcpNMR Analysis (11). The following delay times were used. $FBP21^{326–376}$ T_1 (s): 0.08, 0.64, 0.4, 0.24, 0.88, 0.08, 0.16, 0.88, 0.24, and 1.6. $FBP21^{326–376}$ T_2 (s): 1, 0.016, 0.32, 0.144, 0.8, 0.016, 0.64, 0.32, 0.48, and 0.64. $FBP21^{326–376}$/$Brr2^{C\text{-}Sec63}$ T_1 (s): 2, 0.08, 0.64, 0.4, 0.24, 0.88, 0.08, 1.28, 0.88, and 0.24. $FBP21^{326–376}$/$Brr2^{C\text{-}Sec63}$ T_2 (s): 0.52, 0.016, 0.032, 0.112, 0.048, 0.016, 0.32, 0.048, 0.064, and 0.112, as well as 0.08, 0.016, 0.032, 0.048, 0.016, 0.032, 0.064, and 0.024 to confirm the very short T_2 times in the bound state. Uncertainties of T_1/T_2 ratios are obtained by error propagation. The overall rotational correlation time (τ_c) was estimated based on the formula $\tau_c = (6 \times T_1/T_2 - 7)^{1/2}/4\pi\nu_N$).

Chemical shift differences were calculated using the formula $\Delta\delta(^1H,^{15}N) = (\delta(^1H)^2 + (0.15 \times \delta(^{15}N))^2)^{1/2}$. Because most residues in $^{15}N\text{-}FBP21^{326–376}$ displayed very large shifts upon binding to $Brr2^{C\text{-}Sec63}$, shift differences were considered significant if they exceeded the average (0.27 ppm), and shifts bigger than >0.1 ppm were considered weakly affected. NMR experiments of $^{15}N\text{-}Brr2^{C\text{-}Sec63}$ with FBP21 proteins were performed in 10 mM Tris, 100 mM NaCl (pH 7.5), and shift differences were considered significant if they exceeded the average plus SD of the experiment with a twofold molar excess of FBP21$^{326–376}$ (0.16 ppm).

For paramagnetic relaxation enhancement (PRE) experiments, purified FBP21^{S344C} and FBP21^{S366C} were reduced with 10 mM dithiothreitol for 1 h at room temperature and afterwards reacted with the nitroxide spin label S-(1-oxyl-2,2,5,5-tetramethyl-2,5-dihydro-1H-pyrrol-3-yl)methyl methanesulfonothioate (MTSL). MTSL-labeling of FBP21$^{S344C-MTSL}$ and FBP21$^{S366C-MTSL}$ was confirmed by mass spectrometry. The peak intensity in ^{1}H-^{15}N-TROSY-HSQC spectra of ^{15}N-Brr2$^{C-Sec63}$ in an equimolar complex with FBP21$^{S344C-MTSL}$ or FBP21$^{S366C-MTSL}$ was compared in their paramagnetic and diamagnetic states, which were achieved by addition of a fivefold molar excess of sodium ascorbate.

Chemical-shift-based secondary structure prediction

To perform chemical-shift-based secondary structure prediction, Cα and Cβ chemical shifts were corrected for the impact of deuteration in IDPs, whereas CO, H^N, and N^H chemical shifts were left uncorrected as described in (12). The Cα secondary chemical shift was calculated by comparing the measured deuterium-corrected shifts with sequence-specific random-coil shifts obtained by the web tool ncIDP, which uses an IDP library and applies neighbor correction (13). The deviation of measured Cα shifts from expected random-coil values indicates the presence of α-helical (positive deviation) or β-sheet/extended conformations (negative deviation).

The presence of stable secondary structure elements was also predicted by using the web tool CSI3.0 (14). Here, secondary structure is predicted based on deuterium-corrected (12) Cα and Cβ, as well as CO, H^N, and N^H chemical shifts in a program pipeline combining CSI2.0 (15) to calculate secondary shifts based on reference random-coil shifts derived from the database RefDB (16), RCI (17) to determine stably folded regions with order parameters >0.7, TALOS-N (18) to derive torsion angles for the stable regions, and side-chain RCI (19) to determine side-chain mobility. The combined output is used to assign different types of secondary structure.

The propensity to form transiently structured elements was calculated with the web tool ncSPC (20) based on deuterium-corrected (12) Cα and Cβ, as well as CO, H^N, and N^H chemical shifts. The program builds on the originally published secondary structure propensity score (21) and incorporates the sequence-specific neighbor-corrected random-coil chemical shifts (13) as reference. The comparison of measured chemical shifts to these random-coil reference values and to values corresponding to fully formed structural elements derived from RefDB (16) leads to an ncSPC score with values between -1 and 0, indicating propensity for β-sheet formation, and between 0 and 1 for α-helix formation.

Docking and energy minimization to generate a model of the complex

The CABS-dock server (http://biocomp.chem.uw.edu.pl/CABSdock) (22) was used to dock various fragments of FBP21$^{326–376}$ to Brr2$^{C-Sec63}$ (Protein Data Bank (PDB): 4f91 (23)). Regions not shifting in NMR experiments were selected as unlikely to bind, and the fragment's secondary structure predicted from NMR chemical shifts was included in the docking protocol. After the implementation of side-chain contact information in 2018 (24), we docked overlapping fragments of the maximal allowed length of 30 residues (FBP21$^{326–355}$, FBP21$^{337–366}$, and FBP21$^{347–376}$), including the two most prominent cross-links (FBP21-K338/Brr2$^{C-Sec63}$-K1874 and FBP21-K365/Brr2$^{C-Sec63}$-K2087) previously detected between FBP21$^{200–376}$ and Brr2 (9) as soft distance restraints. It has been shown that it is appropriate to constrain the distance between Lys-Cα-atoms to 26–30 Å in molecular dynamics simulations if the 11 Å cross-linker BS3 was used (25). Here, we decided to use a distance of 10 Å between the lysine pairs because a coarse-grained model is used, the restraint is soft, and larger distances lead to altogether even fewer models compatible with the chemical shift data. To optimize the resulting models, we docked the same fragments, including the restraints derived from cross-linking, and additionally included contact information from NOEs (6 Å between the residue pairs FBP21–351/353 and FBP21–364/366) and contact information to guide the N-terminal segment based on chemical shift data (8 Å between residue pairs FBP21-F337/Brr2$^{C-Sec63}$-Q1870 and FBP21-K334/Brr2$^{C-Sec63}$-E1864).

To derive models of the entire FBP21$^{326–376}$ in complex with Brr2$^{C-Sec63}$, models best consistent with experimental data were selected from the CABS-dock run including contact information from cross-linking, from NOEs, and for the N-terminal segment. These models were combined using the MODELER software (26,27) by connecting residues 326–337 of the models obtained with the N-terminal fragment to residues 338–363 of the models obtained with the central fragment to residues 364–376 of the models obtained with the C-terminal fragment in the following combinations. N-terminal-central-C-terminal model: 1-5-1, 2-9-4, 3-10-1, 4-5-2, 5-9-1, 6-10-4, 7-5-7, 8-9-2, 9-10-4, and 10-5-7. The resulting complexes were energy minimized by 3000 steps of steepest descent minimization using Ambertools16 (28). The interface area was calculated by the difference between the sum of the surface-accessible areas (SASA) of the artificial monomers and the SASA of the complex. SASAs were calculated in pymol with the default probe radius of 1.4 Å.

RESULTS

The 50 C-terminal residues of FBP21 (FBP21$^{326–376}$) are intrinsically disordered

From previous experiments (9), we had already assumed that FBP21$^{276–376}$ is intrinsically disordered. To get more detailed information about the conformational and dynamic behavior of FBP21$^{326–376}$ in the free state as well as upon binding to Brr2$^{C-Sec63}$, NMR experiments were performed with uniformly ^{2}H-^{15}N-^{13}C-labeled FBP21$^{326–376}$ in solution. The ^{1}H-^{15}N-TROSY-HSQC spectrum of FBP21$^{326–376}$ showed very low chemical shift dispersion, consistent with an IDPR, as seen in Fig. 1 *A*.

Standard 3D experiments were used to confidently assign all the non-proline-backbone resonances except for 360R, 363N, and 367R. These latter residues are part of a region that displays very low peak intensities (Fig. S1), which complicate backbone assignments because of reduced spectral quality.

The presence of secondary structure in free FBP21$^{326–376}$ was investigated by analyzing Cα secondary shifts: we compared deuteration-corrected (12) measured ^{13}Cα chemical shifts to neighbor-corrected sequence-specific random-coil values that we obtained by the ncIDP web interface (13). As shown in Fig. 2 *A* (*blue bars*), there is no indication for a stable secondary structure in free FBP21$^{326–376}$. Additionally, we used the web tool CSI3.0 (14) to predict the secondary structure for free FBP21$^{326–376}$ based on all assigned chemical shifts including H^N, N^H, Cα, Cβ, and CO. Again, no stably formed secondary structure elements are present in free FBP21$^{326–376}$ (Fig. 2 *B*, *line* CSI3.0 (free)). However, RefDB reference chemical shifts used by CSI3.0 are derived only from folded proteins, and no sequence neighbor

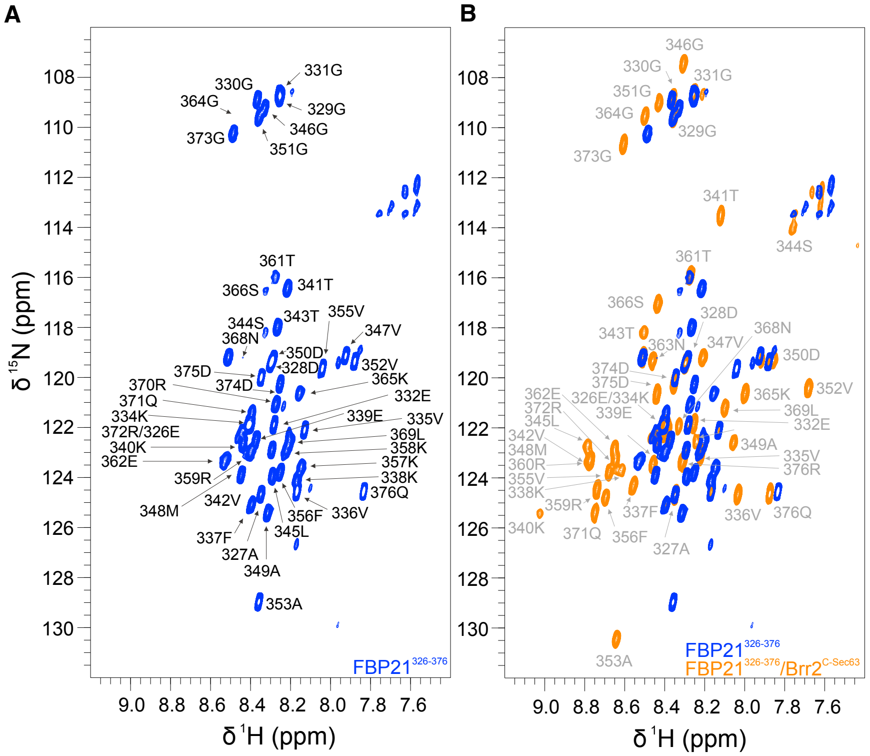

FIGURE 1 Backbone assignment of free and Brr2$^{\text{C-Sec63}}$-bound FBP21$^{326–376}$. (*A*) Shown is the assigned ^{1}H-^{15}N-TROSY-HSQC of 140 μM ^{2}H-^{15}N-^{13}C-FBP21$^{326–376}$ with low signal dispersion, indicating intrinsic disorder. (*B*) An overlay of ^{1}H-^{15}N-TROSY-HSQC spectrum of 140 μM FBP21$^{326–376}$ alone and in complex with a threefold molar excess of Brr2$^{\text{C-Sec63}}$. Assigned peaks deriving from FBP21$^{326–376}$ in the Brr2$^{\text{C-Sec63}}$-bound state are labeled in gray. To see this figure in color, go online.

correction is applied, both being important for the analysis of IDP chemical shifts. Additionally, secondary structure elements might transiently form and thus escape the scoring for stably formed secondary structure in CSI3.0. Therefore, we investigated transient secondary structure formation using the web tool ncSPC (20), which uses sequence-specific neighbor-corrected reference random-coil shifts derived from ncIDP (13). The ncSPC score yields information about the propensity for transient secondary structure formation in values between -1 (100% β-sheet) and $+1$ (100% α-helix). Values close to zero as observed for free FBP21$^{326–376}$ (Fig. 2 *C*, *blue bars*) indicate no propensity for secondary structure formation. The only residues showing a propensity toward a defined conformation were residues 335–338. For these, we observed on average a 14% propensity to populate an extended conformation. This might reflect the sequence composition of that region: residues 335–337 (VVF) form the longest stretch of order-promoting residues (29) in the entire protein fragment.

Taken together, free FBP21$^{326–376}$ does not adopt a stable secondary structure and shows only a very small stretch with a slightly enlarged propensity for transient population of an extended conformation.

Nearly all residues of FBP21$^{326–376}$ are involved in the interaction with Brr2$^{\text{C-Sec63}}$

Having characterized free FBP21$^{326–376}$, we were interested in learning more about how this protein covers the large binding site on Brr2$^{\text{C-Sec63}}$ described in (9) and whether this goes along with folding into a defined conformation. The ^{1}H-^{15}N-TROSY-HSQC spectrum of free FBP21$^{326–376}$ was compared to a spectrum in the presence of a threefold molar excess of Brr2$^{\text{C-Sec63}}$ (Fig. 1 *B*).

Extensive chemical shift differences of nearly all residues were detectable for FBP21$^{326–376}$ upon binding to Brr2$^{\text{C-Sec63}}$. This appears to be in contrast with the small number of chemical shift changes that we reported previously for FBP21$^{276–376}$ (9). However, strong differences in peak intensity as well as a higher number of peaks in the larger fragment resulted in masking of the effects that can be observed with the shorter fragment. For both proteins, the interaction occurs in the slow-to-intermediate exchange regime with respect to the NMR time (Fig. S2 *A*; (9)). Interpretation of the large chemical shift differences required de novo assignment of the bound state. By using standard triple resonance experiments, we could obtain the backbone assignment of all nonproline residues except for Lys358 (Fig. 1 *B*).

Because of the large amount of strong chemical shift differences, any value bigger than the average (0.27 ppm) was considered significant (Fig. 3 *A*), and residues with shifts >0.1 ppm were considered weakly affected. We identified two regions where significant shifts cluster (338–359 and 368–372) and found that the N-terminal residues 326–334 are hardly affected.

Thus, nearly the complete FBP21$^{326–376}$ was involved in or at least affected by the interaction with Brr2$^{\text{C-Sec63}}$. This

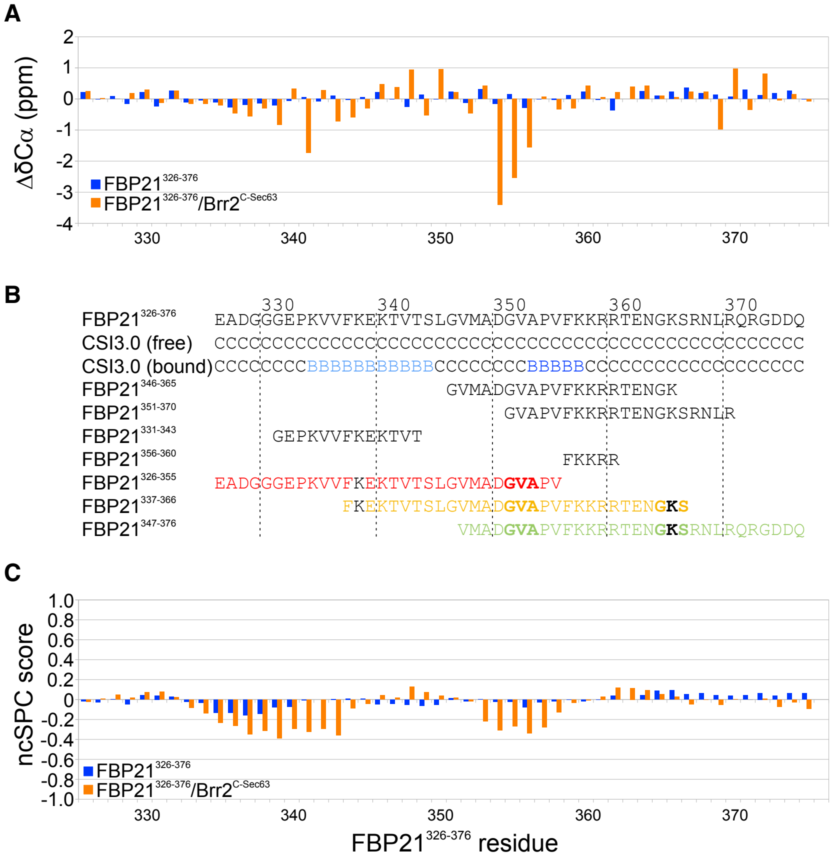

FIGURE 2 Secondary structure analysis of free and Brr2$^{C-Sec63}$-bound FBP21$^{326–376}$. (*A*) Cα secondary chemical shifts are shown for free and Brr2$^{C-Sec63}$-bound FBP21$^{326–376}$. Fluctuation around zero indicates no defined secondary structure in free FBP21$^{326–376}$. In the Brr2$^{C-Sec63}$-bound state, increased negative values indicate regions adopting an extended conformation. (*B*) The secondary structure was predicted for free and Brr2$^{C-Sec63}$-bound FBP21$^{326–376}$ by using the web tool CSI3.0 (14). Free FBP21$^{326–376}$ is predicted to be disordered (CSI3.0 free), whereas the Brr2$^{C-Sec63}$-bound state appears to form regions with extended conformation (CSI3.0 bound, *light B*: interior β-strand, *dark B*: edge β-strand). Additionally shown are peptide fragments of FBP21$^{326–376}$ investigated here and/or previously (9). Peptides only used for docking analyses are colored as in Fig. S5, with lysine residues in black indicating the positions of restraints derived from cross-linking and residues in bold indicating the position of restraints derived from NOEs. (*C*) The secondary structure propensity score (ncSPC score: value 1 corresponds to 100% α-helix, value −1 corresponds to 100% β-strand) was calculated for free and Brr2$^{C-Sec63}$-bound FBP21$^{326–376}$ by using the web tool ncSPC (20). To see this figure in color, go online.

clearly supports the observation that the highly positive stretch FKKRR (FBP21$^{356–360}$, $K_D = 20 \pm 1$ μM) that is necessary for the interaction is not sufficient to obtain the full affinity of FBP21$^{326–376}$ ($K_D = 0.11 \pm 0.001$ μM) (9). In our previous publication, longer fragments (for sequence, see Fig. 2 *B*) including the FKKRR motif were also investigated for binding, and it was found that FBP21$^{346–365}$ (peptide 57, $K_D = 27.5 \pm 2.2$ μM) (9) did not lead to a gain in affinity with respect to the FKKRR motif, although it covers more residues with significant chemical shift differences. This indicates that these residues lack higher affinity motifs. An alternative charged C-terminal extension of the FKKRR stretch (FBP21$^{351–370}$, peptide 58) in contrast yielded a 15-fold higher affinity ($K_D = 1.3 \pm 0.2$ μM) (9). Because residues 368–370 display elevated chemical shift differences (Fig. 3 *A*), this peptide indeed appears to add another region directly involved in binding, although the important charged motif likely extends further and covers FPB21 residues 367–372 (RNLRQR) as based on the chemical-shift-difference data (Fig. 3 *A*). This extension, however, was not enough to reach the 10-fold higher affinity achieved by the full FBP21$^{326–376}$ fragment. The additional affinity is likely mainly contributed by residues 338–345, which were not part of any of the previously investigated peptides but display many significant chemical shift changes upon binding to Brr2$^{C-Sec63}$.

We therefore tested a peptide covering part of this region (FBP21$^{331–343}$; for sequence, see Fig. 2 *B*) for binding by NMR spectroscopy. Even after addition of a 20-fold molar excess of peptide, all chemical shift differences in ^{1}H-^{15}N-TROSY-HSQC spectra of Brr2$^{C-Sec63}$ remained far below the significance cutoff of full-length FBP21$^{326–376}$ (Fig. S2, *B* and *E*), speaking against specific binding of FBP21$^{331–343}$. The peptide covers the only short motif in free FBP21$^{326–376}$ that displayed a slight propensity for transient extended conformation in the ncSPC score (Fig. 2 *C*, *blue bars*). It might thus act as a weak β-type molecular recognition feature (β-MoRF) (30), in which a low-populated extended conformation is selected and driven into the fully extended state in the complex. Such a scenario would likely depend on energy provided by the charged motifs.

Thus, the interaction of unfolded FBP21$^{326–376}$ and Brr2$^{C-Sec63}$ is not fully explainable by the additive combination of the affinities of individual peptidic epitopes present in free unfolded FBP21$^{326–376}$.

FBP21$^{326–376}$ wraps around Brr2$^{C-Sec63}$ in an extended conformation

The clearly increased signal dispersion in ^{1}H-^{15}N-TROSY-HSQC spectra of Brr2$^{C-Sec63}$-bound FBP21$^{326–376}$ as compared to the free protein (Fig. 1 *B*) supports the idea

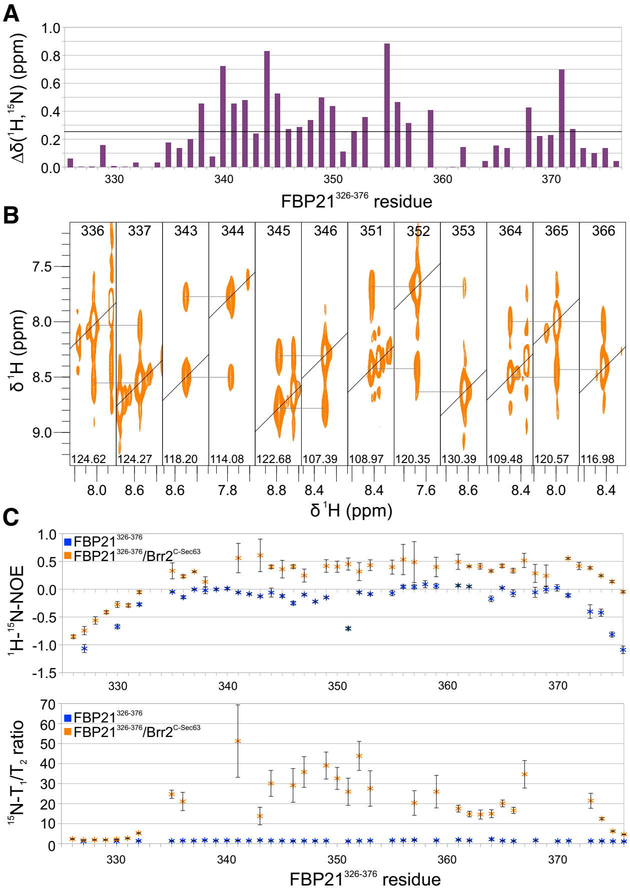

FIGURE 3 Differences in fold and dynamics between free and Brr2$^{C\text{-}Sec63}$-bound FBP21$^{326\text{–}376}$. (*A*) Plotted are per-residue combined ^1H,^{15}N chemical shift differences between the two spectra shown in Fig. 1 *B*. The black line indicates the average chemical shift difference (0.27 ppm). (*B*) Strips of a $^1H\text{-}^{15}N$-NOESY-HSQC spectrum of 140 μM $^2H\text{-}^{15}N\text{-}^{13}C$-FBP21$^{326\text{–}376}$ in the presence of 420 μM Brr2$^{C\text{-}Sec63}$ show H^N-H^N-NOEs. (*C*) Heteronuclear $^1H\text{-}^{15}N$-NOE values and T_1/T_2 relaxation time ratios obtained for 125 μM ^{15}N-FBP21$^{326\text{–}376}$ without or with a threefold molar excess of unlabeled Brr2$^{C\text{-}Sec63}$. Heteronuclear $^1H\text{-}^{15}N$-NOE values represent the average of three independent measurements, error bars reflect the standard deviation. Uncertainties of T_1 and T_2 times were obtained from exponential fits. To see this figure in color, go online.

of increased order in the bound state, although chemical shift dispersion remains smaller than expected for a fully folded protein. We therefore tested for secondary structure formation in FBP21$^{326\text{–}376}$ upon binding to Brr2$^{C\text{-}Sec63}$ by using Cα secondary chemical shifts and by employing the web tool CSI3.0 for stable and the web tool ncSPC for transient secondary structure formation (Fig. 2, *A–C*). For Brr2$^{C\text{-}Sec63}$-bound FBP21$^{326\text{–}376}$, CSI3.0 assigns an extended/β-strand conformation to two regions (extended region I includes residues 334–344, and extended region II includes residues 353–357; Fig. 2 *B*). The assignment of interior and edge β-strand by CSI3.0, which is based on the effect of H-bond formation on chemical shifts as well as the length of the folded structure (14), might overinterpret flexible IDP structures and could thus represent an extended backbone conformation instead of a proper β-strand. The existence of the extended region I is not immediately evident from Cα secondary chemical shifts (Fig. 2 *A*) but is well detected by the web tool ncSPC, indicating a population of, on average, 28% transient structure formation (Fig. 2 *C*). Extended region I might therefore be less stably folded than extended region II, which is clearly detectable in both Cα secondary chemical shifts and ncSPC (Fig. 2, *A* and *C*).

To get more information on potential 3D structure formation in the Brr2$^{C\text{-}Sec63}$-bound FBP21$^{326\text{–}376}$, we performed $^1H\text{-}^{15}N$-NOESY-HSQC spectra of the free and the bound state. Stable α-helical regions should result in sequential $H^N(i)\text{-}H^N(i+1)$ and $H^N(i)\text{-}H^N(i+2)$ NOEs. Only few short-range backbone $H^N(i)\text{-}H^N(i+1)$ NOEs were detectable in the bound state (Fig. 3 *B*), whereas no $H^N(i)\text{-}H^N(i+1)$ NOEs were seen in free FBP21$^{326\text{–}376}$ (Fig. S3). In agreement with the secondary structure prediction, these data rule out the formation of α-helical elements but add information to the two extended regions: the H^N-H^N-NOE between residue 336 and 337 is located in the center of extended region I and suggests a distorted extended conformation rather than a continuous straight β-strand. The strong backbone H^N-H^N-NOEs between residues 343 and 344 and between 345 and 346 as well as 351, 352, and 353 speak for a turn or bend conformation between the extended regions. NOEs between residues 364, 365, and 366 indicate another turn or bend right in front of the second charged motif FBP21$^{367\text{–}372}$ (RNLRQR) that adds affinity to the interaction.

The formation of a β-sheet in contrast to a single-strand or extended region would result in strong interstrand NOEs that should be detectable either in between distal FBP21$^{326\text{–}376}$-H^N protons or, in the case of sheet complementation, by a strand formed by Brr2$^{C\text{-}Sec63}$ in between H^N(FBP21$^{326\text{–}376}$) and H^N(FBP21$^{326\text{–}376}$) protons. Both are not detectable here, speaking against the formation of a stable β-sheet. The presence of weak, transient contacts, however, cannot be excluded.

Based on the combination of chemical shifts, secondary structure prediction, and NOEs, we suggest that the N-terminus of FBP21$^{326\text{–}376}$ is not involved in binding. The following distorted extended stretch adds affinity but energetically depends on the interaction of the two charged motifs, the extended strand/FKKRR motif, which is followed by a bend/turn and the RNLRQR motif.

FBP21$^{326\text{–}376}$ retains dynamics upon interaction with Brr2$^{C\text{-}Sec63}$

Having characterized charged elements as well as folding into extended strands to contribute to the FBP21$^{326\text{–}376}$/Brr2$^{C\text{-}Sec63}$ interaction, we were interested in the dynamic nature of the complex.

Fast internal protein dynamics contribute most to the entropy of a protein or a complex. The ^{1}H-^{15}N-heteronuclear NOE (hetNOE) is very sensitive to a protein's fast internal dynamics and is thus suitable for investigating flexibility in intrinsically disordered proteins (31). We measured ^{1}H-^{15}N-hetNOE values for free and Brr2$^{\text{C-Sec63}}$-bound FBP21$^{326\text{–}376}$ (Fig. 3 *C*, *top*).

Free FBP21$^{326\text{–}376}$ displays high internal dynamics with an average hetNOE value of -0.07 ± 0.14 for the core residues 334–372 and with highly flexible tails as indicated by large negative hetNOE values. In agreement with the secondary structure prediction results, there is no indication for a transiently or stably folded region, which would be expected to display hetNOE values between 0.4 and 0.7 or >0.7, respectively. Additionally, we measured T_1 and T_2 relaxation times (Fig. S4 *A*). For globular, rigid proteins in the slow-motion regime, the average T_1/T_2 ratio can be used to estimate the overall rotational correlation time (τ_c). For IDPs, anisotropic tumbling as well as exchange contributions to T_2 complicate matters (32). A plot of T_2 over T_1 (Fig. S4 *B*), however, indicates that the core residues of free FBP21$^{326\text{–}376}$ appear to tumble isotropically with flexible tails. The T_1/T_2 ratios (Fig. 3 *C*, *bottom*) are consistently very small, with an average of 1.5 for the core residues 334–372. Assuming rigid and isotropic tumbling, this would correspond to a τ_c of 1.7 ns, which is small even for a 5.8 kD protein and thus consistent with intrinsic disorder.

Upon binding to Brr2$^{\text{C-Sec63}}$, hetNOE values of FBP21$^{326\text{–}376}$ increase similarly over the entire sequence of the protein to an average value of 0.39 ± 0.11 for core residues 334–372. This overall increase likely contains a contribution because of the slower tumbling of the protein as part of the complex and thus speaks against independent tumbling of individual FBP21$^{326\text{–}376}$ regions except for the N-terminal tail, which retains strongly negative hetNOE values. Despite this apparent "tumbling as a complex," the average hetNOE of FBP21$^{326\text{–}376}$ does not reach values above 0.7 as observed for folded regions in free Brr2$^{\text{C-Sec63}}$ (average hetNOE 0.76 ± 0.19) and as expected for a stably folded complex of 40 kD. This implies remaining dynamic disorder even in the bound state, as has been observed in other IDPs upon complex formation (33). This observation is also supported by T_1 and T_2 relaxation times. T_1 times increase modestly upon complex formation, whereas T_2 times drastically drop for most regions in FBP21$^{326\text{–}376}$ (Fig. S4 *A*), possibly indicating an exchange contribution in the bound state. The plot of T_2 over T_1 (Fig. S4 *B*) shows an anisotropic pattern. This might reflect the extended conformation of FBP21$^{326\text{–}376}$ as well as remaining dynamics in the bound state. T_1/T_2 ratios (Fig. 3 *C*, *bottom*) fluctuate between 10 and 70 for core residues 334–372. However, because of weak peak intensities (Fig. S1) and signal overlap, hardly any reliable value could be obtained for residues 334–343 (extended region I), 353–356 (extended region II), and 368–372 (second charged motif). Thus, the average T_1/T_2 value of 26.4 for core residues 334–372 mainly represents the flexibly bound elements. T_1/T_2 ratios of N-terminal residues 326–332 remain small in the bound state, supporting the hypothesis that the N-terminus is not involved in the interaction. Also, residues in between the two charged motifs (363–366) and C-terminal residues (373–376) display reduced T_1/T_2 ratios (16.4 ± 1.9 and 11.2 ± 6.6, respectively), indicating remaining dynamics.

The observed relaxation behavior is supported by a variation in the intensity of the FBP21$^{326\text{–}376}$-H$^{\text{N}}$ to water-proton crosspeaks detected in the NOESY spectrum (Fig. S5). These signals likely result from water/protein NOEs and/or direct or indirect exchange with water protons. The pattern of these signals appears consistent with amide-proton protection from the bulk solvent water in the binding site: amide protons of the N-terminal residues 326–331 display strong signals to water protons, possibly indicating high solvent accessibility. In contrast to that, the extended regions I and II and the two charged motifs do not appear to be solvent accessible, whereas the bend connecting the two charged motifs (residues 361–366) as well as the very C-terminal residues (373–376) appear to be slightly more solvent exposed.

Thus, FBP21$^{326\text{–}376}$ appears to remain dynamic in complex with Brr2$^{\text{C-Sec63}}$.

Model of the FBP21$^{326\text{–}376}$/Brr2$^{\text{C-Sec63}}$ complex

Because attempts to crystallize the complex failed, a model of the FBP21$^{326\text{–}376}$/Brr2$^{\text{C-Sec63}}$ complex was generated. We used the web server CABS-dock (22,24) for docking of FBP21 fragments to the structure of Brr2$^{\text{C-Sec63}}$ (PDB: 4f91 (23)). Initially, we docked the fragments for which experimental data are available: the peptides FBP21$^{331\text{–}343}$, FBP21$^{346\text{–}365}$, and FBP21$^{351\text{–}370}$ and the FKKRR motif (FBP21$^{356\text{–}360}$) (for sequences, see Fig. 2 *B*). Despite marking regions displaying no chemical shift difference as unlikely to bind and including the fragment's secondary structure obtained from NMR chemical shifts, this resulted in variable binding sites and binding modes (Fig. S6 *A*).

Thus, we decided to dock longer overlapping fragments of the maximal allowed length of 30 residues covering the entire sequence of FBP21$^{326\text{–}376}$ (for sequences, see Fig. 2 *B*). Additionally, we included the two most prominent cross-links previously detected between FBP21$^{200\text{–}376}$ and Brr2 (9) as soft restraints with a distance of 10 Å between the residue pairs FBP21-K338/Brr2$^{\text{C-Sec63}}$-K1874 and FBP21-K365/Brr2$^{\text{C-Sec63}}$-K2087 to account for the cross-linker length. Thus, we docked the central 30 residues FBP21$^{337\text{–}366}$ (including both cross-linking constraints) as well as the 30 N-terminal (FBP21$^{326\text{–}355}$) and the 30 C-terminal residues (FBP21$^{347\text{–}376}$), each including one of the cross-linking constraints (for sequences, see

Fig. 2 *B*). This resulted in better-defined binding sites (Fig. S6 *B*). The binding mode (Fig. S6 *B*, *blue arrow*)—in which FBP21$^{326–376}$ binds the Brr2$^{C\text{-}Sec63}$-helical bundle (HB) domain with its N-terminus, then funnels through the groove between HB, helix-loop-helix (HLH), and immunoglobulin-like (IG) domains and folds up on the HLH domain to insert its C-terminus between the HLH and IG domains—is the only one detected here that is overall consistent with chemical shift data, the extended secondary structure prediction, and cross-linking results.

Looking at the models in more detail, $H^N(i)$-$H^N(i + 1)$ NOEs detected in FBP21$^{326–376}$ in the bound state (Fig. 3 *B*) are not adequately reflected. Because the CABS-dock procedure does not allow for inclusion of distance restraints between individual atoms, we decided to softly restrain the distance between the center of mass of residue pairs FBP21–351/353 as well as FBP21–364/366 to 6 Å because we could detect consecutive NOEs for these residues (Fig. 3 *B*). Additionally, the N-terminus and extended region I dock to very variable binding modes. This might properly reflect weak interactions, consistent with the observation that the peptide covering extended region I (FBP21$^{331–343}$) does not interact on its own (Fig. S2). An arrangement in which the extended region I aligns toward the bottom of the HB domain, as seen only in one of the models (Fig. S6 *B*, *black arrow*), would, however, be much more consistent with the observation of strong chemical shifts at the bottom of the Brr2$^{C\text{-}Sec63}$-HB domain and no chemical shifts between Brr2$^{C\text{-}Sec63}$-HB and -IG domain upon binding to FBP21$^{326–376}$ ((9); Fig. 4 *A*). Additionally, besides the cross-link to K1874 located in the Brr2$^{C\text{-}Sec63}$-HB domain, which we used to guide the docking, FBP21-K338 has also been found to cross-link to K1567 located in the Brr2^{C}-RecA unit (9) (Fig. S7). To account for these experimental evidences, we additionally introduced soft distance restraints of 8 Å between residue pairs FBP21-F337/Brr2$^{C\text{-}Sec63}$-Q1870 and FBP21-K334/Brr2$^{C\text{-}Sec63}$-E1864 to guide the extended region I to the bottom of the HB domain. In combination with the NOE restraints mentioned above, docking of the N-terminal, central, and C-terminal 30-residue fragments of FBP21$^{326–376}$ resulted in an overall similar general binding mode as before but an N-terminal arrangement more consistent with the experimental data (Fig. S5 *C*).

Based on this last docking run, we extracted individual models matching best the experimental data and connected docking results for FBP21-residues 326–337 (N-terminal fragment) to results for residues 338–363 (central fragment) and these to results for residues 364–376 (C-terminal fragment) in combinations in which the termini match best. Energy minimization resulted in 10 models for full-length FBP21$^{326–376}$ in complex with Brr2$^{C\text{-}Sec63}$ (Fig. 4 *A*). With an average value of 4608 ± 280 Å^2, the 10 models cover a large interface wrapping around the HLH domain in a distorted extended conformation in overall agreement with experimental data available for Brr2$^{C\text{-}Sec63}$ (9) and obtained for FBP21$^{326–376}$ here. In Fig. 4 *A*, Brr2$^{C\text{-}Sec63}$ is shown in surface representation, with residues displaying chemical shifts color coded according to the different fragments of FBP21$^{326–376}$ inducing the shifts upon binding (9). Models agree with the observation that the N-terminal part of FBP21$^{326–376}$, including the extended region I, mainly induces shifts in the HB domain, whereas the central part covered by peptide FBP21$^{346–365}$ appears to attach to the HLH domain, and only C-terminal residues (as in peptide FBP21$^{351–370}$ or full-length FBP21$^{326–376}$) induce shifts in the groove between the IG and HLH domains. The nine N-terminal FBP21 residues flexibly protrude at the bottom of the HB domain in agreement with experimental data, indicating no participation in the interaction. Residues 335–344 do not adopt a continuous but a distorted extended conformation, providing a structure that appears consistent with a combination of the extended secondary structure prediction and the measured $H^N(i)$-$H^N(i + 1)$ NOE. The bend arrangement of the residues 345–352 connecting the two extended regions is overall consistent with measured $H^N(i)$-$H^N(i + 1)$ NOEs. The extended region II then positions the important FKKRR motif between two negatively charged patches on the HLH and IG domains as proposed previously (9). The adjacent stretch of residues 361–367 displays a relatively variable, exposed bend conformation in overall agreement with reduced T_1/T_2 ratios and increased NOEs to water. The following stretch (residues 368–372), which clearly adds to affinity (9), feeds in a groove between the HLH and IG domains consistent with chemical shift differences upon binding and reduced NOEs to water, whereas the very C-terminal residues 373–376 appear to display a more variable arrangement.

To test the model, we performed PRE experiments. Serine 344 and 366 of FBP21$^{326–376}$ were individually mutated to cysteine, and a nitroxide spin label (MTSL) was attached to these residues, resulting in the proteins FBP21$^{S344C\text{-}MTSL}$ and FBP21$^{S366C\text{-}MTSL}$, which were added to ^{15}N-Brr2$^{C\text{-}Sec63}$ in equimolar amounts. We compared peak intensities in ^{1}H-^{15}N-TROSY-HSQC spectra of the complexes with the MTSL in the paramagnetic and the diamagnetic states, which were induced by the addition of ascorbate. Spectra of the complexes in the diamagnetic state were very similar to the spectrum with equimolar amounts of wild-type FBP21$^{326–376}$, indicating that the modifications do not abrogate binding. Nitroxide spin labels typically lead to relaxation enhancement within a radius of ~20 Å, resulting in loss of peak intensity. Here, we measured the loss of peak intensity in Brr2$^{C\text{-}Sec63}$ amide peaks upon complex formation with the spin-labeled FBP21$^{326–376}$ (Figs. 4, *B–E* and S8). In the case of both complexes, the average peak intensity ratio was 0.94, with distinct peaks showing significant relaxation enhancement as indicated in the structure of Brr2$^{C\text{-}Sec63}$ in Fig. 4, *D* and *E*. In the case of FBP21$^{S366C\text{-}MTSL}$ (Fig. 4 *E*), the

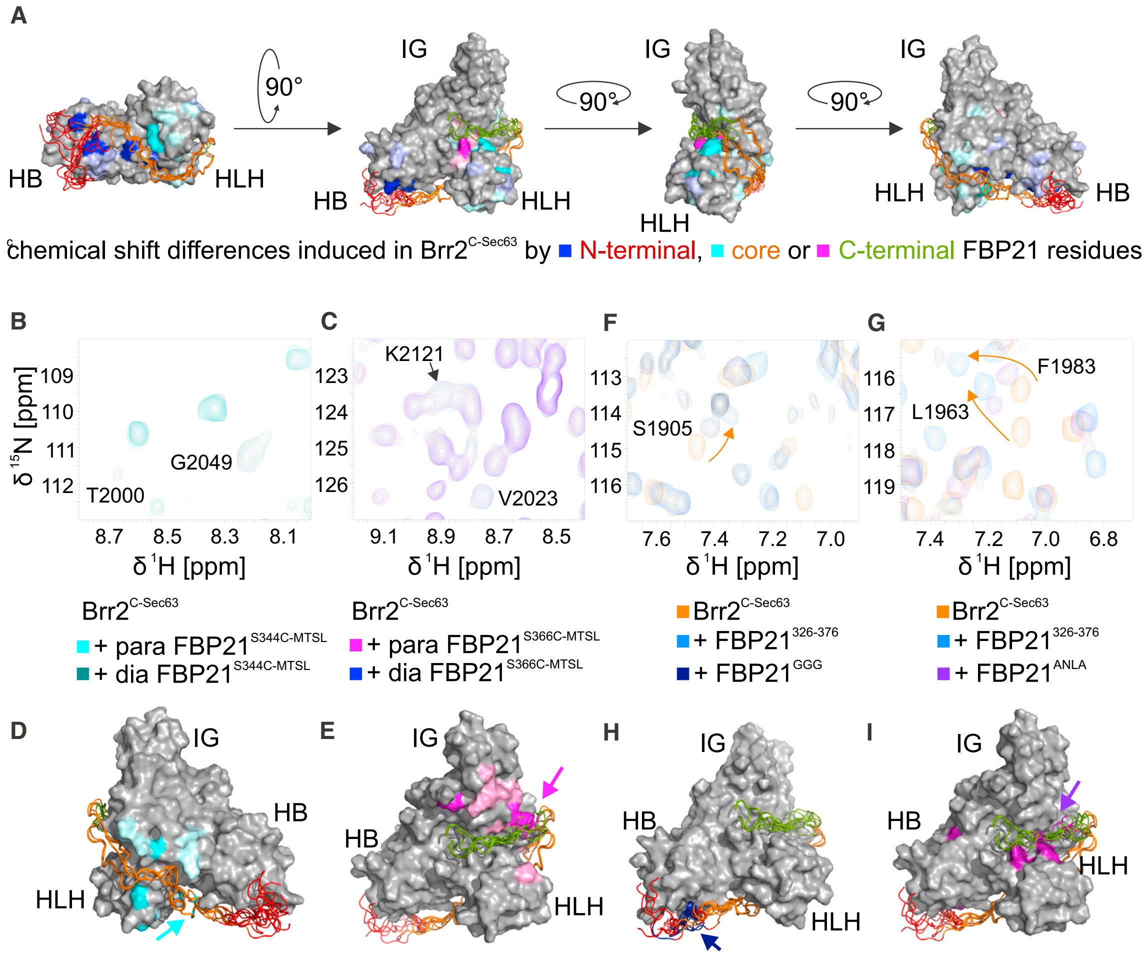

FIGURE 4 Energy-minimized models generated from docking results (Fig. S6 *C*). (*A*) Models of FBP21$^{326–376}$ are shown with Brr2$^{\text{C-Sec63}}$ in surface representation. Residues showing chemical shift differences upon addition of FBP21$^{326–376}$ (9) are shown in strong (if bigger than mean + 1 SD) or light (if between mean and mean + 1 SD) colors. Chemical shift differences are induced by N-terminal residues (that is upon interaction with FBP21$^{326–376}$ but not with N-terminally truncated fragments) by core residues (that is upon interaction with FBP21$^{326–376}$, FBP21$^{346–365}$, and FBP21$^{351–370}$) or by C-terminal residues (that is upon interaction with FBP21$^{326–376}$ or FBP21$^{351–370}$). (*B–E*) PRE experiments confirm the models. (*B*) and (*C*) show regions of the overlay of ^{1}H-^{15}N-TROSY-HSQC spectra of 100 μM ^{15}N-Brr2$^{\text{C-Sec63}}$ in complex with equimolar amounts of (*B*) FBP21$^{\text{S344C-MTSL}}$ and (*C*) FBP21$^{\text{S366C-MTSL}}$ in its paramagnetic and its diamagnetic states. (*D*) and (*E*) illustrate the position of the label in the models (*arrows*) of FBP21$^{326–376}$ and regions experiencing relaxation enhancement in Brr2$^{\text{C-Sec63}}$ in surface representation. Indicated is a loss in peak intensity beyond the average minus SD (67%) or beyond 25% in light or dark colors respectively. (*F–I*) Mutations introduced in FBP21 confirm the models. (*F*) and (*G*) show regions of the overlay of ^{1}H-^{15}N-TROSY-HSQC spectra of 100 μM ^{15}N-Brr2$^{\text{C-Sec63}}$ free in complex with a twofold molar excess of FBP21$^{326–376}$ and a twofold molar excess of (*F*) FBP21$^{\text{GGG}}$ or (*G*) FBP21$^{\text{ANLA}}$. (*H*) and (*I*) show Brr2$^{\text{C-Sec63}}$ for which chemical shift differences upon complex formation with FBP21$^{\text{GGG}}$ (*H*) or FBP21$^{\text{ANLA}}$ (*I*) drops beyond the significance cutoff in the presence of the mutations. The position of the mutations in FBP21$^{326–376}$ are indicated with an arrow. PDB: 4f91 (23) is used to present Brr2$^{\text{C-Sec63}}$ with models of FBP21$^{326–376}$. To see this figure in color, go online.

distance between the backbone of residue FBP21–366 in the model and the residues experiencing relaxation enhancement in Brr2$^{\text{C-Sec63}}$ is always smaller than 30 Å and matches expectations from the models. In the case of FBP21$^{\text{S344C-MTSL}}$ (Fig. 4 *D*), most effected residues are in proximity to the postulated position of FBP21–344 and locate to the HLH domain. We would, however, also have expected to see an effect at the bottom of the HB domain. This might indicate that residue 344 is positioned closer toward the HLH domain than the model implies. Additionally, individual residues experiencing relaxation enhancement are up to 40 Å away, indicating either a higher mobility or a slightly different position of residue FBP21–344.

In addition to the PRE experiments, we also introduced mutations in FBP21$^{326–376}$. By mutating FBP21 residues 334–336 from KVV to GGG (FBP21$^{\text{GGG}}$), we intended to confirm the postulated position of this motif in the model and also investigate the impact of the small hydrophobic patch VVF on the interaction because we postulated above that it might act as weak β-MoRF. ^{1}H-^{15}N-TROSY-HSQC spectra of ^{15}N-Brr2$^{\text{C-Sec63}}$ in the presence of a twofold molar excess of FBP21$^{\text{GGG}}$ are very similar to the spectrum with a twofold molar excess of wild-type protein FBP21$^{326–376}$, with average chemical shift differences of 0.066 and 0.064, respectively (Figs. 4 *F* and S2, *C* and *E*). Only for two Brr2$^{\text{C-Sec63}}$ residues do chemical shift differences between the free and the bound state drop beyond the significance cutoff (Fig. S2 *E*). These residues locate to the expected position in Brr2$^{\text{C-Sec63}}$ according to the models (Fig. 4 *H*). The overall minor impact on the interaction, and especially the lack of a stronger influence on Brr2 residues contacting the extended region I, rather speaks against a β-MoRF hypothesis, and we conclude that residues 334–336 are not essential for the interaction.

We also targeted the second charged motif (RNLRQR) by mutating FBP21-residues R367 and R370 to alanine (FBP21$^{\text{ANLA}}$). These mutations lead to a clearly reduced average chemical shift difference of 0.039 ppm as compared to wild-type FBP21$^{326\text{–}376}$ (Fig. S2 *E*). Brr2$^{\text{C-Sec63}}$ residues close to the postulated position of FBP21 residues R367 and R370 show drastically reduced chemical shift differences between free and bound states (Fig. 4, *E* and *I*). This confirms the overall position of the second charged motif in the models and also implies that removal of the two positive charges interferes with binding of the second charged motif but does not abrogate the interaction with the rest of FBP21$^{326\text{–}376}$.

PRE experiments, as well as mutations introduced in FBP21$^{326\text{–}376}$, are overall consistent with the postulated models. These models, however, should neither be seen as representing the full conformational space sampled by the complex nor taken as accurate structural models with atomic resolution. They illustrate the experimental results and provide a structural solution for the complex without excluding other solutions that might well agree with experimental data because the dynamic nature of the complex might be consistent with an ensemble of conformations.

In summary, we provide an example of how the combination of conformational and dynamic information derived from NMR spectroscopy and fragment docking can be used to model the behavior of a dynamic complex between an intrinsically disordered spliceosomal accessory protein with a highly conserved and stably folded spliceosomal core protein. Our data reveal that FBP21$^{326\text{–}376}$ covers the large interface on Brr2$^{\text{C-Sec63}}$ by wrapping around the HLH domain yet keeping essential dynamic features.

DISCUSSION

Here, we used NMR-spectroscopy to characterize changes in conformation and dynamics of FBP21$^{326\text{–}376}$ upon binding to Brr2$^{\text{C-Sec63}}$ and combined the results with fragment-based docking to derive structural models of the complex.

In our models (Fig. 4 *A*), the nine N-terminal residues do not participate in the interaction. The remaining 42 residues, however, appear to contribute to the interaction in several not merely additive motifs without the formation of stable secondary structure elements and retaining a certain amount of dynamics: the distorted extended region I of FBP21$^{326\text{–}376}$ attaches to the Brr2$^{\text{C-Sec63}}$-HB domain and feeds through the groove between Brr2$^{\text{C-Sec63}}$-HB/IG/HLH domains. The extended region II/FKKRR motif that had been shown to be mainly responsible for the interaction affinity (9) wraps around the HLH domain to position the positive charges between negative patches on the Brr2$^{\text{C-Sec63}}$-HLH and -IG domains. After an exposed turn, the second charged motif (RNLRQR) that had been shown to add affinity (9) binds in a groove between Brr2$^{\text{C-Sec63}}$-HLH and -IG domains.

The interaction described here represents an example in which an IDPR covers a large interface on a folded protein in an extended conformation to form a dynamic complex of relatively high affinity.

In comparison to other IDP/ordered-protein complexes, which often display at least small and transient helical elements as, for example, in (33,34), the extended conformation detected in the Brr2$^{\text{C-Sec63}}$-bound state of FBP21$^{326\text{–}376}$ is unusual. Similar arrangements, however, have been observed, for example, for a complex involving a short IDPR of 11 residues (35) but also for a larger interface involving a 30-residue IDP fragment (36). Recently, a very high-affinity extended complex has been observed to form between two IDPs that both remain disordered upon binding (37), indicating that extended fuzzy complexes do not contradict high affinity.

The K_D-value of 0.11 ± 0.001 μM (9) observed for the FBP21$^{326\text{–}376}$/Brr2$^{\text{C-Sec63}}$ complex speaks for a relatively high but not unusual affinity as compared to other IDP/ordered-protein complexes (38). The high affinity likely results from binding enthalpy provided by the interface, which is unusually large (38) with ~4608 Å^2 as derived from the average of the energy-minimized models. The complex might also benefit from increased on rates as postulated by the "fly-casting" mechanism (39), which claims a larger capture radius of IDPs, especially acting on charge interactions as, for example, that of the FKKRR and the second charged motif (RNLRQR).

The ^{1}H-^{15}N-hetNOE values obtained for the complex do not reach the values expected for stably bound elements as, for example, observed for the binding of transiently folded helical elements (33,34), and T_1/T_2 ratios remain relatively low. This speaks for remaining dynamics in the bound state (33,40). In more detail, the N-terminal tail displays dynamic properties similar to the free protein and the C-terminal residues as well as the region between the two charged motifs show more than average flexibility. In contrast to that, we can assume that the two charged motifs are relatively stably bound, whereas binding of the extended region I appears to depend on the interaction of the charged motifs but not so much on the presence of the short hydrophobic patch and might adopt a looser orientation, as implied by the PRE experiments. Dynamic disorder in the N-terminal region might also be reflected by the variable cross-linking positions detected for FBP21-K338 (Fig. S6). Taken together, the FBP21$^{326–376}$/Brr2$^{C-Sec63}$-complex fulfils prerequisites for a flanking as well as polymorphic model of a fuzzy complex (2). The N-terminal residues, however, might only remain flexible in the FBP21$^{326–376}$ fragment under investigation. In the context of a longer construct like FBP21$^{276–376}$, which is capable of reducing Brr2 unwinding activity based on further contacts, these residues might as well be kept in a more stable arrangement.

IDPs/IDPRs are suggested to save space inside molecular machines because they can form large interfaces without adding much volume (4). This might well apply to the dense environment of the spliceosome, for which an unusually high percentage of disorder has been described (5), but also raises the question why the FBP21$^{326–376}$/Brr2$^{C-Sec63}$-interaction invests in such a complex interface and high affinity.

FBP21 has been shown to reduce human Brr2 helicase unwinding activity by the combination of two mechanisms (9): binding of FBP21$^{276–376}$ interferes with the activating interaction (23) of catalytically inactive Brr2^{CC} with catalytically active Brr2^{NC}. Additionally, an interaction with U4/U6 di-snRNA depending on residues FBP21$^{200–376}$ interferes with unwinding activity by depleting the available pool of U4/U6 di-snRNA (9). If this interaction happens to delay U4/U6 unwinding, leaving the spliceosome in a position awaiting activation (10), it appears conceivable that the affinity of the complex should not be too low to reliably keep it in the stalled state. Thus, the FBP21$^{326–376}$/Brr2$^{C-Sec63}$ interaction might well contribute initial affinity to the interaction and properly position the two proteins for further essential contacts happening outside FBP21$^{326–376}$ because this fragment neither binds RNA nor is sufficient to reduce Brr2 unwinding activity (9).

The advantage of having an IDP as a regulator in signaling processes has often been suggested to lie in their low affinity and still-high specificity to allow for a transient enough interaction to fulfill the prerequisites of reversible signaling (3). Such a situation might apply to another regulator of Brr2 unwinding activity: the yeast protein Ntr2 interacts with the yeast-Brr2$^{C-Sec63}$ unit but with a K_D value of only 14 ± 1 μM and more reminiscent of a peptidic rather than a large interface (41). Here, the observed large interface in combination with the relatively high affinity argues for another scenario in which tight binding asks for strong regulatory cues needed to break the FBP21$^{326–376}$/Brr2$^{C-Sec63}$ interaction to allow for full Brr2 unwinding activity, for example, upon transition to the B^{act} complex.

Regulation of the inhibiting interaction of FBP21$^{326–376}$ with Brr2$^{C-Sec63}$ appears feasible by mechanisms interfering with the physicochemical properties of the IDPR. Phosphorylation, for example, is a post-translational modification often seen to regulate IDP interactions (42,43). The introduction of a negative charge by phosphorylation of FBP21$^{326–376}$ can be anticipated to interfere with the interaction of the important positively charged FKKRR motif with patches of negatively charged residues in Brr2$^{C-Sec63}$. This is also supported by the clear reduction in affinity induced by mutation of FKKRR to FEKER (9). Indeed, phosphorylation sites are predicted theoretically, albeit with relatively low scores and contradicting results from two programs: the best scoring phosphorylation site predicted by the server NetPhos3.1 (44) is a PKC-mediated threonine phosphorylation site (score 0.529) directly C-terminal to the FKKRR motif (KKRR**T**ENGK). The DISPHOS 1.3 server (45), which also takes disorder prediction into account, yields the best score (0.550) for a serine phosphorylation in the exposed turn preceding the important C-terminal motif ENGK**S**RNLR. In both situations, phosphorylation of FBP21$^{326–376}$ could well interfere with essential charge interactions, critically reducing the affinity of the interaction so that it can easily be released. Indeed, previous proteomics experiments had revealed an interaction of SRPK2 kinase with the WW domains of FBP21 (46), conceivably enabling the placement of the kinase in the vicinity of the putative phosphorylation site. SRPK2 has been shown to phosphorylate Prp28, thereby allowing it to associate firmly with the U4/U6-U5 tri-snRNP and fostering B complex formation. The SRPK2 protein plays a role in the phosphorylation of other spliceosomal proteins (e.g., SF2), but once confirmed, FBP21 would, to our knowledge, be the first described B^{act} complex protein to be regulated by this kinase.

An alternative mode of regulation common to IDPs (47) that may act concomitantly or independent of phosphorylation is proline *cis-trans* isomerization. Peptidyl-prolyl *cis-trans* isomerase H, a known component of the U4/U6 snRNP (6), was found as an interaction partner of FBP21 (9). There are only two proline residues in FBP21$^{326–376}$, one of them in the N-terminal region and one close to the FKKRR motif—the conformation of both might be relevant for positioning either the N-terminus or the FKKRR element in a functionally correct position.

In summary, structural information is still rare on highly dynamic IDP/ordered-protein complexes because of their fuzzy nature limiting experimental approaches. Here, we show how the combination of conformational and dynamic restraints derived from NMR spectroscopy in combination with fragment docking leads to models describing how an IDPR dynamically covers a large folded interface in an extended conformation.

SUPPORTING MATERIAL

Eight figures are available at http://www.biophysj.org/biophysj/supplemental/S0006-3495(18)34418-7.

AUTHOR CONTRIBUTIONS

J.S., M.B., J.R.L., and L.M.H. performed the biochemical and NMR experiments. J.S. and E.T.A. performed the docking and energy minimization of the model. J.S., M.B., L.M.H., E.T.A., and C.F. contributed to the planning, analysis, and interpretation of the results. J.S. wrote the manuscript with input from all authors.

ACKNOWLEDGMENTS

We thank Peter Schmieder and Monika Beerbaum (Leibniz-Forschungsinstitut für Molekulare Pharmakologie [FMP] Berlin) for pulse sequences and NMR technical support.

This work was supported by a Deutsche Forschungsgemeinschaft grant to C.F. (Collaborative Research Center SFB765 (Project C4)). The BioSupraMol Core Facility is supported by the Deutsche Forschungsgemeinschaft.

REFERENCES

1. Dyson, H. J., and P. E. Wright. 2005. Intrinsically unstructured proteins and their functions. *Nat. Rev. Mol. Cell Biol.* 6:197–208.
2. Tompa, P., and M. Fuxreiter. 2008. Fuzzy complexes: polymorphism and structural disorder in protein-protein interactions. *Trends Biochem. Sci.* 33:2–8.
3. Tompa, P. 2002. Intrinsically unstructured proteins. *Trends Biochem. Sci.* 27:527–533.
4. Gunasekaran, K., C. J. Tsai, …, R. Nussinov. 2003. Extended disordered proteins: targeting function with less scaffold. *Trends Biochem. Sci.* 28:81–85.
5. Korneta, I., and J. M. Bujnicki. 2012. Intrinsic disorder in the human spliceosomal proteome. *PLoS Comput. Biol.* 8:e1002641.
6. Wahl, M. C., C. L. Will, and R. Lührmann. 2009. The spliceosome: design principles of a dynamic RNP machine. *Cell.* 136:701–718.
7. Laggerbauer, B., T. Achsel, and R. Lührmann. 1998. The human U5-200kD DEXH-box protein unwinds U4/U6 RNA duplices in vitro. *Proc. Natl. Acad. Sci. USA.* 95:4188–4192.
8. Raghunathan, P. L., and C. Guthrie. 1998. RNA unwinding in U4/U6 snRNPs requires ATP hydrolysis and the DEIH-box splicing factor Brr2. *Curr. Biol.* 8:847–855.
9. Henning, L. M., K. F. Santos, …, C. Freund. 2017. A new role for FBP21 as regulator of Brr2 helicase activity. *Nucleic Acids Res.* 45:7922–7937.
10. Bertram, K., D. E. Agafonov, …, H. Stark. 2017. Cryo-EM structure of a pre-catalytic human spliceosome primed for activation. *Cell.* 170:701–713.e11.
11. Vranken, W. F., W. Boucher, …, E. D. Laue. 2005. The CCPN data model for NMR spectroscopy: development of a software pipeline. *Proteins.* 59:687–696.
12. Maltsev, A. S., J. Ying, and A. Bax. 2012. Deuterium isotope shifts for backbone ^{1}H, ^{15}N and ^{13}C nuclei in intrinsically disordered protein α-synuclein. *J. Biomol. NMR.* 54:181–191.
13. Tamiola, K., B. Acar, and F. A. Mulder. 2010. Sequence-specific random coil chemical shifts of intrinsically disordered proteins. *J. Am. Chem. Soc.* 132:18000–18003.
14. Hafsa, N. E., D. Arndt, and D. S. Wishart. 2015. CSI 3.0: a web server for identifying secondary and super-secondary structure in proteins using NMR chemical shifts. *Nucleic Acids Res.* 43:W370–W377.
15. Hafsa, N. E., and D. S. Wishart. 2014. CSI 2.0: a significantly improved version of the chemical shift index. *J. Biomol. NMR.* 60:131–146.
16. Zhang, H., S. Neal, and D. S. Wishart. 2003. RefDB: a database of uniformly referenced protein chemical shifts. *J. Biomol. NMR.* 25:173–195.
17. Berjanskii, M. V., and D. S. Wishart. 2005. A simple method to predict protein flexibility using secondary chemical shifts. *J. Am. Chem. Soc.* 127:14970–14971.
18. Shen, Y., and A. Bax. 2013. Protein backbone and sidechain torsion angles predicted from NMR chemical shifts using artificial neural networks. *J. Biomol. NMR.* 56:227–241.
19. Berjanskii, M. V., and D. S. Wishart. 2013. A simple method to measure protein side-chain mobility using NMR chemical shifts. *J. Am. Chem. Soc.* 135:14536–14539.
20. Tamiola, K., and F. A. Mulder. 2012. Using NMR chemical shifts to calculate the propensity for structural order and disorder in proteins. *Biochem. Soc. Trans.* 40:1014–1020.
21. Marsh, J. A., V. K. Singh, …, J. D. Forman-Kay. 2006. Sensitivity of secondary structure propensities to sequence differences between alpha- and gamma-synuclein: implications for fibrillation. *Protein Sci.* 15:2795–2804.
22. Kurcinski, M., M. Jamroz, …, S. Kmiecik. 2015. CABS-dock web server for the flexible docking of peptides to proteins without prior knowledge of the binding site. *Nucleic Acids Res.* 43:W419–W424.
23. Santos, K. F., S. M. Jovin, …, M. C. Wahl. 2012. Structural basis for functional cooperation between tandem helicase cassettes in Brr2-mediated remodeling of the spliceosome. *Proc. Natl. Acad. Sci. USA.* 109:17418–17423.
24. Kurcinski, M., M. Blaszczyk, …, S. Kmiecik. 2017. A protocol for CABS-dock protein-peptide docking driven by side-chain contact information. *Biomed. Eng. Online.* 16 (*Suppl 1*):73.
25. Merkley, E. D., S. Rysavy, …, J. N. Adkins. 2014. Distance restraints from crosslinking mass spectrometry: mining a molecular dynamics simulation database to evaluate lysine-lysine distances. *Protein Sci.* 23:747–759.
26. Webb, B., and A. Sali. 2014. Protein structure modeling with MODELLER. *Methods Mol. Biol.* 1137:1–15.
27. Webb, B., and A. Sali. 2017. Protein structure modeling with MODELLER. *Methods Mol. Biol.* 1654:39–54.
28. Case, D. A., D. S. Cerutti, …, P. A. Kollman. 2017. AMBER 2017. University of California, San Francisco, CA.
29. Romero, P., Z. Obradovic, …, A. K. Dunker. 2001. Sequence complexity of disordered protein. *Proteins.* 42:38–48.
30. Vacic, V., C. J. Oldfield, …, A. K. Dunker. 2007. Characterization of molecular recognition features, MoRFs, and their binding partners. *J. Proteome Res.* 6:2351–2366.
31. Dyson, H. J., and P. E. Wright. 2004. Unfolded proteins and protein folding studied by NMR. *Chem. Rev.* 104:3607–3622.
32. Salvi, N., A. Abyzov, and M. Blackledge. 2017. Atomic resolution conformational dynamics of intrinsically disordered proteins from NMR spin relaxation. *Prog. Nucl. Magn. Reson. Spectrosc.* 102-103:43–60.
33. Berlow, R. B., H. J. Dyson, and P. E. Wright. 2017. Hypersensitive termination of the hypoxic response by a disordered protein switch. *Nature.* 543:447–451.
34. Aitio, O., M. Hellman, …, P. Permi. 2012. Enterohaemorrhagic Escherichia coli exploits a tryptophan switch to hijack host f-actin assembly. *Structure.* 20:1692–1703.
35. Selenko, P., G. Gregorovic, …, M. Sattler. 2003. Structural basis for the molecular recognition between human splicing factors U2AF65 and SF1/mBBP. *Mol. Cell.* 11:965–976.
36. Bhattacharyya, R. P., A. Reményi, …, W. A. Lim. 2006. The Ste5 scaffold allosterically modulates signaling output of the yeast mating pathway. *Science.* 311:822–826.
37. Borgia, A., M. B. Borgia, …, B. Schuler. 2018. Extreme disorder in an ultrahigh-affinity protein complex. *Nature.* 555:61–66.
38. Teilum, K., J. G. Olsen, and B. B. Kragelund. 2015. Globular and disordered-the non-identical twins in protein-protein interactions. *Front. Mol. Biosci.* 2:40.
39. Shoemaker, B. A., J. J. Portman, and P. G. Wolynes. 2000. Speeding molecular recognition by using the folding funnel: the fly-casting mechanism. *Proc. Natl. Acad. Sci. USA.* 97:8868–8873.

40. Andresen, C., S. Helander, …, M. Sunnerhagen. 2012. Transient structure and dynamics in the disordered c-Myc transactivation domain affect Bin1 binding. *Nucleic Acids Res.* 40:6353–6366.

41. Wollenhaupt, J., L. M. Henning, …, M. C. Wahl. 2018. Intrinsically disordered protein Ntr2 modulates the spliceosomal RNA helicase Brr2. *Biophys. J.* 114:788–799.

42. Csizmok, V., A. V. Follis, …, J. D. Forman-Kay. 2016. Dynamic protein interaction networks and new structural paradigms in signaling. *Chem. Rev.* 116:6424–6462.

43. Bah, A., R. M. Vernon, …, J. D. Forman-Kay. 2015. Folding of an intrinsically disordered protein by phosphorylation as a regulatory switch. *Nature.* 519:106–109.

44. Blom, N., S. Gammeltoft, and S. Brunak. 1999. Sequence and structure-based prediction of eukaryotic protein phosphorylation sites. *J. Mol. Biol.* 294:1351–1362.

45. Iakoucheva, L. M., P. Radivojac, …, A. K. Dunker. 2004. The importance of intrinsic disorder for protein phosphorylation. *Nucleic Acids Res.* 32:1037–1049.

46. Klippel, S., M. Wieczorek, …, C. Freund. 2011. Multivalent binding of formin-binding protein 21 (FBP21)-tandem-WW domains fosters protein recognition in the pre-spliceosome. *J. Biol. Chem.* 286:38478–38487.

47. Follis, A. V., F. Llambi, …, R. W. Kriwacki. 2015. Pin1-Induced proline isomerization in cytosolic p53 mediates BAX activation and apoptosis. *Mol. Cell.* 59:677–684.